

Structural origins of the low-temperature orthorhombic to low-temperature tetragonal phase transition in high- T_c cuprates – Supplementary Information

Jeremiah P. Tidey,¹ Christopher Keegan,² Nicholas C. Bristowe,³ Arash A. Mostofi,² Zih-Mei Hong,^{4,5} Bo-Hao Chen,⁶ Yu-Chun Chuang,⁶ Wei-Tin Chen,^{4,7} and Mark S. Senn^{1,*}

1. Department of Chemistry, University of Warwick, Gibbet Hill, Coventry, CV4 7AL, United Kingdom

2. Departments of Physics and Materials, and the Thomas Young Centre, Imperial College London, London SW7 2AZ, United Kingdom

3. Centre for Materials Physics, Durham University, South Road, Durham, DH1 3LE, United Kingdom

4. Center for Condensed Matter Sciences and the Center of Atomic Initiative for New Materials, National Taiwan University, Taipei 10617, Taiwan

5. Department of Chemistry, Fu-Jen Catholic University, New Taipei 24205, Taiwan

6. National Synchrotron Radiation Research Center, Hsinchu 30076, Taiwan

7. Taiwan Consortium of Emergent Crystalline Materials, Ministry of Science and Technology, Taipei 10622 Taiwan

Section S1: PXRD refinements

In all refinements of the sample material, La_2MgO_4 , refinements were performed using TOPAS-Academic (version 6) [1] in space group $Pccn$ and raised to the designated symmetry by the implementation of appropriate constraints. Atomic positions were refined by symmetry-adapted displacement formalism [2] as implemented in ISODISTORT (version 6.10.0) [3,4] except where stated otherwise. Isotropic displacement parameters were refined for each element type and with scaling of the axial oxygen by 1.8 times that of the equatorial site, a constraint we have found suitable from other work performed on $n=1$ Ruddlesden-Popper perovskites. Except where explicitly discussed, strain was modelled using a Stephens model [5] of appropriate symmetry. Unless otherwise stated, all refinements are by the Rietveld method and include the refinement of a scale factor for each phase. The background for low temperature series was modelled using 10 terms of a shifted Chebyshev polynomials series to account for broader features due to the capillary / sample environment; 15 terms were used for the high-temperature sweep with the inclusion of a single gaussian function.

For the low temperature data sweep, at 100-300 K, inclusive, the sample was modelled employing two tetragonal phases of identical symmetry ($P4_2/ncm$; “LTT”), unit cell, atomic positional and displacement parameters but with freely-refined Stephens tetragonal strain parameter sets (designated the dual-strained LTT model, “DS-LTT”). A range of similar models were tested for fitting the atypical peak shapes found here, including single-phase systems of LTT and orthorhombic ($Bmab$, “LTO”; $Pccn$, “LTLO”) symmetry, and two-phase systems of inequivalent tetragonal (LTT+LTT’) or tetragonal and orthorhombic (LTT+LTO) symmetries. Examples of the fit to key peaks are provided in Fig. S1 overleaf. Given no significant difference between the latter two, it follows to choose the most simple description, *i.e.*, LTT+LTT’. Yet, while these modelled the peak shape best and provided the lowest fit factors, this provided only a marginal improvement over DS-LTT. Since there is no physically compelling reason to choose two systems of equivalent symmetry and geometry but inequivalent cell parameters in a system devoid of potential chemical inhomogeneity. Hence, since the DS-LTT model only exhibits deficiencies similar in the fit of peak profiles as do the accepted models in the LTO and HTT phases, it is chosen as the final model. Data at 350 and 450 K were then modelled using

a single LTO phase. We note that there appears a small degree of the LTO in the low-temperature sweep data at 300 K but this could not be satisfactorily modelled and the DS-LTT model provided equally as meaningful a result for LTT parameters at this temperature.

For the high-temperature data sweep, at 300 to 340 K, the sample clearly showed a coexistence of phases typical to this first-order phase transformation. Refinement models including a mixture of phases were tested and a DS-LTT+LTO system provided a reasonable fit but structural parameters and also orthorhombic cell parameters were evidently unreasonable and hence are omitted from discussion. Similarly, sample data from 350 to 370 K, inclusive, showed clear deficiencies when modelled as a purely LTO phase and their structural data are omitted. From 400 K, the data were modelled well as a single LTO phase. At and above 620 K, it was necessary to intrinsically constrain related mode amplitudes to minimise the impact of correlation with unmodelled intensity from the impurity phases. This was performed by deriving the ratio of the oxygen components of the X_3^+ mode to the lanthanum components across the preceding, good refinements and refining only a single parameter; no constraints were applied to the Γ_1^+ mode components. Sample data at 950 K and above were refined as a single phase of the $I4/mmm$, "HTT" phase in the F -centred setting for simplicity of the discussion and analysis.

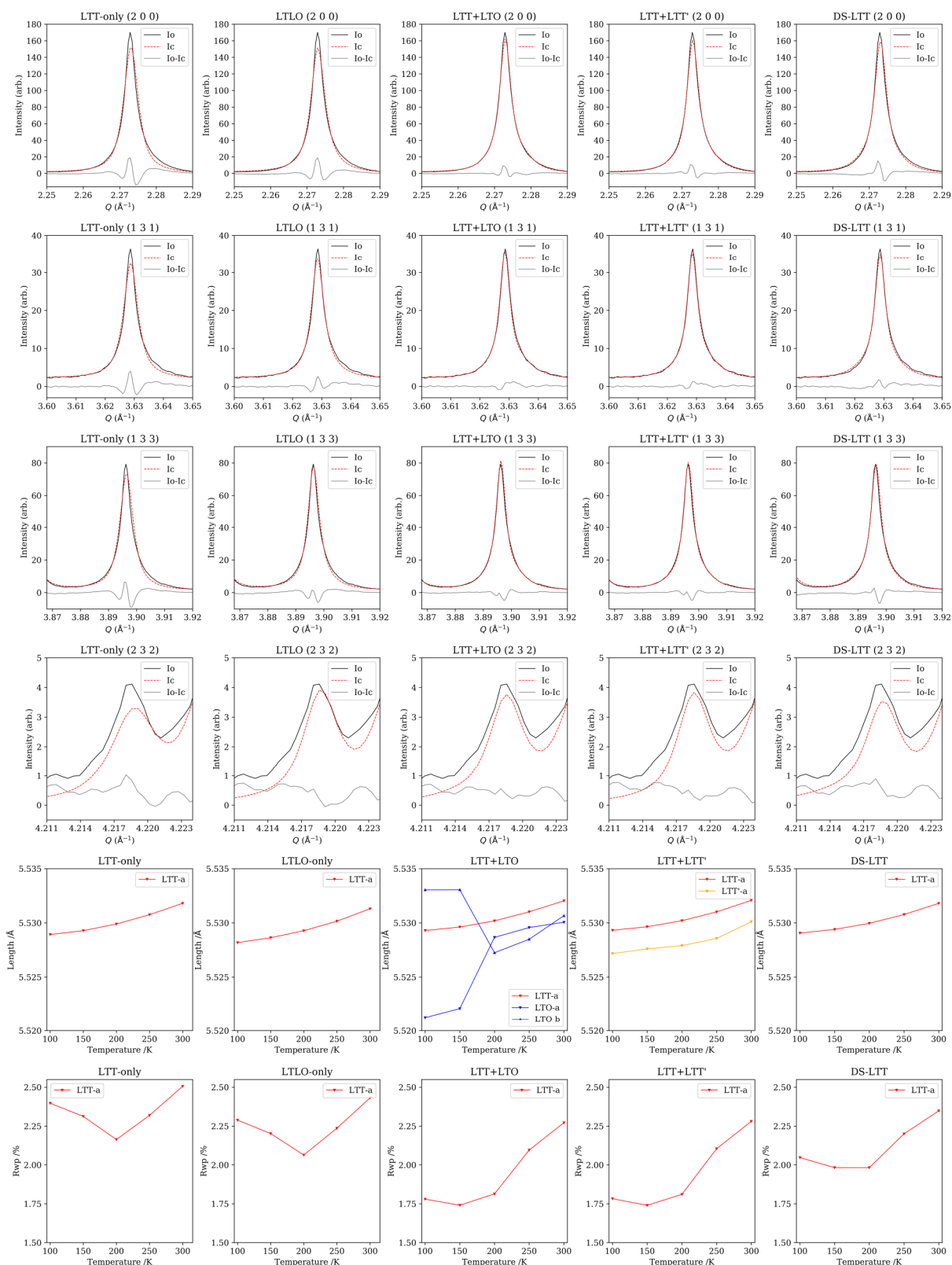


Figure S1. PXRD Rietveld refinement of a given model (columns) fit to specified peaks (rows) at 100 K, as well as plots of the a and b (where relevant) cell parameters as well as R_{wp} for those models.

Throughout the study, the MgO impurity was modelled as the $Fm\bar{3}m$ phase with a single unit cell parameter [$a = 4.21198(7)$ Å at 300 K] and one common atomic displacement parameter. For the low

temperature sweep, a simple Lorentzian model of strain was found to be preferred while in the high-temperature sweep it was found that a domain-size dependant Lorentzian peak shape broadening model was instead necessary to obtain reasonable atomic displacement parameters.

Below 620 K, there exists a $\text{La}(\text{OH})_3$ impurity that was modelled using a $P6_3/m$ phase with refinement of two cell parameters [$a = 6.53272(4)$ Å and $c = 3.85820(4)$ Å at 300 K], two atomic positions (oxygen x and y) and one common displacement parameter; H atom is omitted in this model as elsewhere in the literature owing to the distinct insensitivity of pXRD to such. In the low temperature data, a Stephens description of anisotropic hexagonal strain [5] was performed with additional domain size dependent Lorentzian peak shape broadening found also to benefit the refinement, allowing for reasonable and consistent refinement of atomic parameters in both this phase and in the sample. The same model was successfully implemented up to and including 630 K for the high-temperature data. From 620 K until 780 K, this impurity was seen to transform and is modelled using a Pawley refinement of the known monoclinic $P2_1/m$ phase of $\text{LaO}(\text{OH})$ [$a = 4.4509(3)$ Å, $b = 3.9803(2)$ Å, $c = 6.6051(6)$ Å and $\beta = 111.914(6)$ ° at 650 K] and employing a simple Lorentzian model of strain; the former $\text{La}(\text{OH})_3$ model is no longer implemented above 630 K. From 780 K, La_2O_3 is formed and modelled with the $P3m$ phase using two cell [$a = 3.95894(9)$ Å and $c = 6.1809(2)$ Å at 800 K], two atomic position parameters (z for La and one of the two unique oxygens) and one common atomic displacement parameter. Peak shape broadening for La_2O_3 was modelled using a simple Lorentzian strain function. A second impurity was also formed at around 630 K and is depleted by 970 K but this has precluded identification.

An unfortunate quirk of the system is that peaks from the MgO and lanthanide impurities exist at similar angles as key sample superstructure peaks which help define the magnitude of the X_3^+ distortion. While every effort was made to model the impurities accurately, we acknowledge that this has not been perfectly possible. As a consequence, we expect that intensity from the impurity is bled into the more flexible refinement of those sample peaks and hence that the structural distortions observed are overestimated. This is particularly obvious in Figure 3(c) and (d) in the main text where the structural data extracted from the Rietveld refinement is presented. Specifically, an anomalous hump can be seen between approximately 400 and 600 K. From the different regions of the refinement of the LTO structure showing clear but translated trends (*i.e.*, for regions 370-630 K, 640-770 K and 780+ K), it is unclear what the true values should be. However, an intuitive projection of these would estimate the maximum octahedral tilting to be $4.5 \pm 0.5^\circ$, the Cu-O-Cu buckling to be $174.0 \pm 0.5^\circ$, and the X_3^+ mode amplitude to be 0.30 ± 0.03 Å.

Table S1 below provides key crystallographic parameters for our material, La_2MgO_4 , and for La_2CuO_4 and a selection of relevant dopant compositions of the according lanthanum cuprates to display the broad applicability of the surrogate. While a small impact of the more isotropic Mg^{2+} B -site cation vs. Jahn-Teller distorted Cu^{II} on the cell parameters and bond lengths can be seen, these parameters remain broadly very similar, with an elongated apical B -O bond compared to those of the BO_2 plane and similarly ranging A-O distances.

Table S1 Cell parameters for La₂MgO₄ and select lanthanum cuprate materials from the literature at various temperatures.

System	Phase	T /K	<i>a</i>	<i>b</i>	<i>c</i>
La ₂ MgO ₄	HTT	950	5.556915(7)	5.556915(7)	12.739395(17)
	LTO	400	5.508858(13)	5.558496(13)	12.58972(2)
	LTT	100	5.529061(9)	5.529061(9)	12.52222(2)
La ₂ CuO ₄ [6]	HTT	540	5.384(2)	5.384(2)	13.204(5)
	LTO	295	5.357(2)	5.409(2)	13.144(3)
	LTO	50	5.335	5.42	13.11
La _{1.87} Sr _{0.13} CuO ₄ [6]	HTT	295	5.347(3)	5.347(3)	13.223(5)
	LTO	180	5.3457	5.3393	3.2045
	LTO	22	5.354	5.3288	13.1847
La _{1.475} Nd _{0.4} Sr _{0.125} CuO ₄ [7]	LTO	100	5.31528(7)	5.36900(7)	13.1121(2)
	LTT	10	5.34083(8)	5.34083(8)	13.1063(3)
La _{1.9} Ba _{0.1} CuO ₄ [7]	LTO	91	5.3436(1)	5.3773(1)	13.2386(2)
	LTT	15	5.3548(1)	5.3548(1)	13.2356(3)

Table S2 Key interatomic distances for La₂MgO₄ and select lanthanum cuprate materials from the literature at various temperatures.

System	Phase	T /K	B1-O2	B1-O3	B1-O1	A1-O1	A2-O1	A3-O1	A4-O1	A5-O1
La ₂ MgO ₄	HTT	950	1.96467	1.96467	2.269(3)	2.350(3)	2.8263(5)	2.8263(5)	2.8263(5)	2.8263(5)
	LTO	400	1.9595(4)	1.9595(4)	2.244(3)	2.345(3)	2.581(5)	2.8047(6)	3.070(5)	2.8047(6)
	LTT	100	1.9692(8)	1.95482	2.198(3)	2.390(3)	2.570(3)	2.570(3)	3.045(3)	3.045(3)
La ₂ CuO ₄ [6]	HTT	540	1.9035(5)	1.9035(5)	2.4199(14)	2.3520(15)	2.7559(11)	2.7559(11)	2.7559(11)	2.7559(11)
	LTO	295	1.8937(4)	1.8937(4)	2.4210(10)	2.3487(10)	2.5228(11)	2.73968(15)	2.9649(13)	2.73968(15)
	LTO	50	1.89866	1.89866	2.4419	2.3706	2.4911	2.7439	3.0192	2.7439
La _{1.87} Sr _{0.13} CuO ₄ [6]	HTT	295	1.8905(8)	1.8905(8)	2.3940(11)	2.3763(11)	2.7301(15)	2.7301(15)	2.7301(15)	2.7301(15)
	LTO	180	1.88928	1.88928	2.4145	2.3526	2.6479	2.73159	2.8204	2.73159
	LTO	22	1.88968	1.88968	2.4067	2.3588	2.5820	2.72614	2.8913	2.72614
La _{1.475} Nd _{0.4} Sr _{0.125} CuO ₄ [7]	LTO	100	1.89131(14)	1.89131(14)	2.4052(14)	2.3448(17)	2.527(3)	2.7227(4)	2.965(3)	2.7227(4)
	LTT	10	1.8934(4)	1.88827(3)	2.411(3)	2.341(3)	2.573(3)	2.573(3)	2.897(3)	2.897(3)
La _{1.9} Ba _{0.1} CuO ₄ [7]	LTO	91	1.89656(11)	1.89656(11)	2.421(3)	2.369(3)	2.2573(4)	2.7355(7)	2.926(4)	2.7355(7)
	LTT	15	1.89456(11)	1.89321(3)	2.420(3)	2.374(3)	2.607(2)	2.607(2)	2.874(2)	2.874(2)

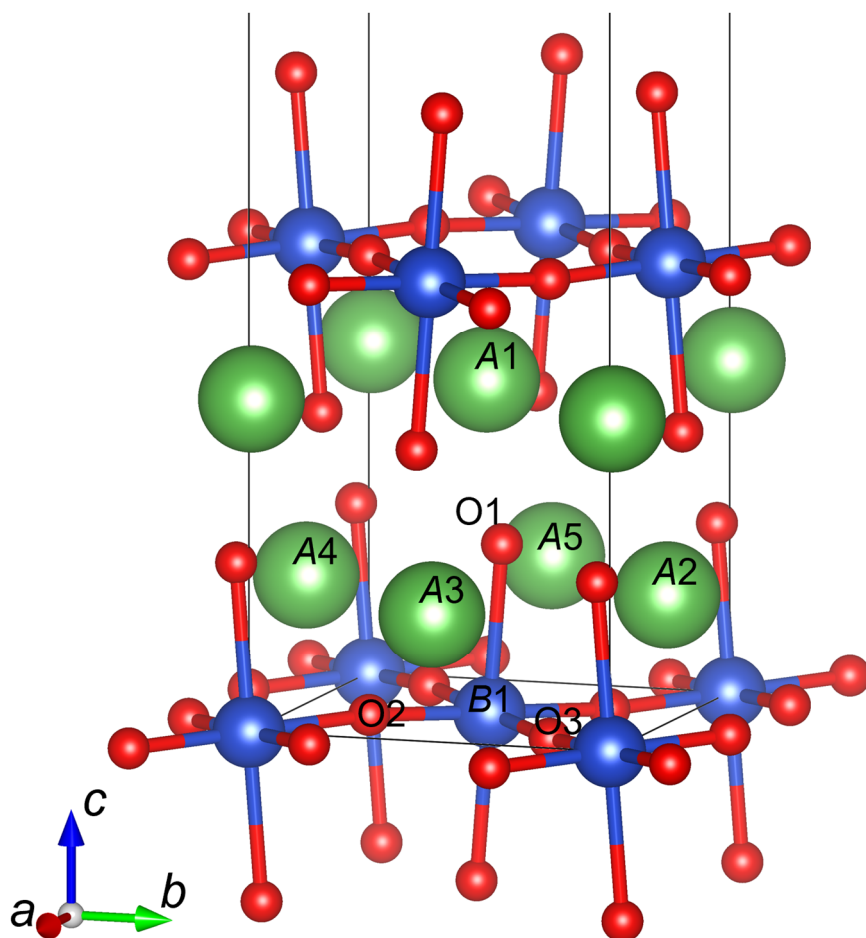


Figure S2 Ball-and-stick depiction of the ‘lanthanum cuprate’ structures discussed, labelled in accordance with Table S2 (specific phase shown, LTO)

Section S2: Computational details for La_2MgO_4 and La_2CuO_4

We used the Quantum ESPRESSO v6.8 plane-wave pseudopotential density functional theory software package for single-point energy calculations and structural relaxations on La_2MgO_4 and v6.7 for La_2CuO_4 [8,9]. For all computations, we approximated the effect of exchange and correlation with the PBEsol functional [10]. The potentials of the ionic cores were approximated using ultrasoft pseudopotentials from the GBRV library (v1.5) generated using the PBEsol functional [11]. We applied an on-site Hubbard U of 4 eV to the La $4f$ orbitals in both compounds and a U of 9 eV to the Cu $3d$ orbitals using the simplified DFT+ U version of Cococcioni and de Gironcoli with atomic projectors [12]. An energy cut-off of 60 Ry was used for the wavefunction expansions, and of 480 Ry for the charge density and potential. The Brillouin zone was sampled using a $5 \times 5 \times 2$ Monkhorst-Pack grid centred on and offset from the Γ point for the $Bmab$ and $P4_2/ncm$ supercells of La_2MgO_4 , an $8 \times 8 \times 4$ grid in the case of La_2CuO_4 , with a commensurate grid for the high-symmetry I/mmm phase.

For La_2CuO_4 , all calculations were performed with collinear spin-polarization, with an anti-ferromagnetic starting magnetization on the Cu atoms. All phases converged to anti-ferromagnetic insulating ground states with an indirect band gap of 2 eV for the $Bmab$ phase.

We first performed structural relaxations on the $I4/mmm$, $Bmab$ and $P4_2/ncm$ structures of La_2BO_4 ($B = \text{Cu}, \text{Mg}$), until the total energy varied by less than 10^{-9} Ry, and the force components and cell pressure were below 10^{-5} Ry/Bohr and 5 MPa, respectively. For the self-consistent field cycles, a convergence tolerance for the total energy of 10^{-10} Ry was used.

We use two methods to generate the single-point energy landscapes associated with the $X_3^+(a; b)$ order parameter (OP) in La_2MgO_4 . In the first method, we use ISODISTORT (version 6.10.0) [3,4] to perform a mode decomposition of the LTO and LTT phases of La_2MgO_4 placed in the $Pccn$ subgroup relative to the relaxed HTT phase in the $I4/mmm$ (no. 139) space-group setting. We obtain vectors for the $X_3^+(a; b)$ and Γ_1^+ modes, where for the LTO phase $b = 0$ and for the LTT phase $b = a$.

We generate a set of interpolated $X_3^+(a; b)$ mode vectors according to the following expression:

$$X_3^+(\rho \cos \theta ; \rho \sin \theta) = \rho(X_3^{+,LTO}(a; 0) \cos 2\theta + X_3^{+,LTT}(a; a) \sin 2\theta) \quad (\text{S1})$$

Where $\rho \geq 0$ and $0 \leq \theta \leq 45^\circ$.

$X_3^{+,LTO}(a; 0)$ and $X_3^{+,LTT}(a; a)$ are the vectors obtained from the mode decomposition of the relaxed LTO and LTT phases, respectively. It is worth noting that the scale parameter, ρ , does not equal the magnitude of the OP since $X_3^{+,LTO}(a; 0)$ and $X_3^{+,LTT}(a; a)$ are not generally orthogonal to one another. This expression enables one to generate structures spanning all possible magnitudes and directions of the OP. For each $Pccn$ structure associated with a particular $X_3^+(a; b)$ vector, we fix the Γ_1^+ mode and lattice strain to those of the relaxed LTO (LTT) phase. This method is used to generate the cuts along the LTO and LTT OP directions of the energy landscape in Figure 4(b) of the main text.

In the second method, we use the relaxed HTT phase in the $Pccn$ space-group setting as the reference structure for the mode decomposition of the relaxed LTO and LTT structures. Since all structures are placed in the same space group, only a $\Gamma_1^{+,Pccn}$ OP is output. This $\Gamma_1^{+,Pccn}$ OP contains both the $X_3^+(a; b)$ OP, the original $\Gamma_1^{+,I4/mmm}$ mode as well as the strain field. For this reason, we label this OP $(X_3^+|\Gamma_1^+)$, since its variation corresponds to the variation of the $X_3^+(a; b)$ OP with simultaneous interpolation of the $\Gamma_1^{+,I4/mmm}$ mode and strain. We use equation (S1), substituting the vectors associated with the $\Gamma_1^{+,Pccn}$ OP for the LTO and LTT phases, to generate a set of interpolated structures spanning the energy landscape associated with the $(X_3^+|\Gamma_1^+)$ OPs. This method is used to generate the energy landscape shown in Figure 4(a) of the main text.

References

- [1] A. A. Coelho, *TOPAS and TOPAS-Academic: An Optimization Program Integrating Computer Algebra and Crystallographic Objects Written in C ++*, J. Appl. Crystallogr. **51**, 210 (2018).

- [2] B. J. Campbell, J. S. O. Evans, F. Perselli, and H. T. Stokes, *Rietveld Refinement of Structural Distortion-Mode Amplitudes*, IUCr Comput. Comm. Newsl. **8**, 81 (2007).
- [3] B. J. Campbell, H. T. Stokes, D. E. Tanner, and D. M. Hatch, *ISODISPLACE: A Web-Based Tool for Exploring Structural Distortions*, J. Appl. Crystallogr. **39**, 607 (2006).
- [4] H. T. Stokes, D. M. Hatch, and B. J. Campbell, *ISODISTORT, ISOTROPY Software Suite*, iso.byu.edu.
- [5] P. W. Stephens, *Phenomenological Model of Anisotropic Peak Broadening in Powder Diffraction*, J. Appl. Crystallogr. **32**, 281 (1999).
- [6] M. Braden, P. Schweiss, G. Heger, W. Reichardt, Z. Fisk, K. Gamayunov, I. Tanaka, and H. Kojima, *Relation between Structure and Doping in $\text{La}_2\text{-xSr}_x\text{CuO}_{4+\delta}$ a Neutron Diffraction Study on Single Crystals*, Phys. C Supercond. Its Appl. **223**, 396 (1994).
- [7] J. D. Axe and M. K. Crawford, *Structural Instabilities in Lanthanum Cuprate Superconductors*, J. Low Temp. Phys. **95**, 271 (1994).
- [8] P. Giannozzi et al., *QUANTUM ESPRESSO: A Modular and Open-Source Software Project for Quantum Simulations of Materials*, J. Phys. Condens. Matter **21**, (2009).
- [9] P. Giannozzi et al., *Advanced Capabilities for Materials Modelling with Quantum ESPRESSO. (ArXiv:1709.10010v1 [Cond-Mat.Mtrl-Sci])*, J. Phys. Condens. Matter **29**, 465901 (2017).
- [10] J. P. Perdew, A. Ruzsinszky, G. I. Csonka, O. A. Vydrov, G. E. Scuseria, L. A. Constantin, X. Zhou, and K. Burke, *Restoring the Density-Gradient Expansion for Exchange in Solids and Surfaces*, Phys. Rev. Lett. **100**, 1 (2008).
- [11] K. F. Garrity, J. W. Bennett, K. M. Rabe, and D. Vanderbilt, *Pseudopotentials for High-Throughput DFT Calculations*, Comput. Mater. Sci. **81**, 446 (2014).
- [12] M. Cococcioni and S. De Gironcoli, *Linear Response Approach to the Calculation of the Effective Interaction Parameters in the LDA+U Method*, Phys. Rev. B - Condens. Matter Mater. Phys. **71**, 1 (2005).